Chem. Mater. **2006,** *18,* 854−860

Local Structures and Raman Spectra in the Ca(Zr,Ti)O_3 Perovskite Solid Solutions

Igor Levin,* Eric Cockayne, Michael W. Lufaso, Joseph C. Woicik, and James E. Maslar

National Institute of Standards and Technology, Gaithersburg, Maryland 20899

Received October 25, 2005. Revised Manuscript Received November 25, 2005

Local structures and cation distributions in perovskite Ca(Zr,Ti)O_3 solid solutions were analyzed using X-ray absorption fine structure and pair-distribution functions obtained from total neutron scattering. The analyses revealed that the Zr−O and Ti−O bond distances in the solid solutions remain distinct and close to their respective values in the end-compounds, $CaZrO_3$ and $CaTiO_3$. The structural strain in the solid solutions, which results from the ionic size mismatch between Zr and Ti, is accommodated by adjustment of the tilting angles for the different [BO_6] octahedra. Additionally, the octahedra are distorted by bending, which affects the O−O distances while preserving a uniform distribution of the B−O distances. Combined experimental and theoretical analyses of Raman spectra demonstrated that high-frequency modes associated with the breathing of oxygen octahedra arise even in the nearly disordered solid solutions. Our results suggest a coexistence of both localized and extended Raman-active breathing vibrations, associated with the octahedra hosting the minority and majority B-cations, respectively. For the dilute solid solutions (<25 at. %), these modes yield two well-resolved Raman peaks.

Introduction

Perovskite solid solutions $(A'A''...)(B'B''...)O_3$ are attractive candidates for use in many electronic applications because of their variable and chemically tunable electronic and magnetic properties. Most materials research to date seeking to understand the crystal-chemical basis of such exploitable properties has been limited to studies of the average structures observed for these compounds.[1] However, numerous indications exist that short-range chemical ordering and local distortions/displacements in perovskite solid solutions significantly affect the useful properties of these materials.[2,3] Local atomic displacements in selected perovskite solid-solution systems have been analyzed using atomic pair-distribution functions (PDF), as derived from total scattering and X-ray absorption fine structure;[4−6] however, quantitative characterization of the short-range chemical ordering in these materials remains a challenge.

Raman spectroscopy has been reported as being a very sensitive probe of B-site ordering, even when this ordering was confined to a nanoscale level, yielding very diffuse superlattice reflections detectable only by electron diffraction.[7−9] Moreover, Raman spectra of perovskite solid solutions with no detectable B-cation ordering, such as $CaZr_{1-x}Ti_xO_3$, contained a high-frequency (700−800 cm^{-1}) peak, which is commonly associated with the presence of B-site ordering in complex perovskites.[10] This vibrational mode, which involves oxygen motion described as symmetric breathing of the [BO_6] octahedra, becomes Raman-active in ordered perovskites ($AB'_{1/2}B''_{1/2}O_3$ or $AB'_{1/3}B''_{2/3}O_3$), where oxygen atoms are bonded to different B-cations.[8] Zheng et al.[10] speculated that the breathing-like mode in the Raman spectra of nominally disordered perovskite solid solutions arises from a nonrandom distribution of the B-cations; in that case, Raman spectroscopy could be used to assess the extent of the short-range B-site ordering. However, the exact origin of the high-frequency Raman peak in the absence of observable long-range or nanodomain ordering remains to be understood. The present contribution reports a combined experimental and theoretical study of local structures, B-cation distribution, and breathing-type oxygen vibrations in nominally disordered $CaZr_{1-x}Ti_xO_3$ solid solutions.

Experimental Section

$CaZr_{1-x}Ti_xO_3$ samples with $x = 0$, 1/12, 1/6, 1/4, 1/3, 1/2, 2/3, 3/4, 11/12, and 1 were prepared by solid-state reaction of $CaCO_3$ (99.999%), ZrO_2, and phosphate-free TiO_2. After an initial calcine at 900 °C, the samples were subjected to multiple heatings at 1550 °C followed by intermediate grindings using an agate mortar and pestle until no changes in the width of the X-ray diffraction reflections could be observed (total heating time ≈ 500 h). X-ray diffraction data for structural refinements were collected using a Siemens D500 powder diffractometer equipped with a Ge mono-

---

* To whom correspondence should be addressed. E-mail: igor.levin@nist.gov.

(1) Mitchell, R. H. *Perovskites: Modern and Ancient*; Almaz Press: Thunder Bay, ON, 2002.
(2) George, A. M.; Iniguez, J.; Bellaiche, L. *Phys. Rev. Lett*. **2003**, *91*, 045504.
(3) Zhou, J. P.; McDevitt, J. T.; Zhou, J. S.; Yin, H. Q.; Goodenough, J. B.; Gim, Y.; Jia, Q. X. *Appl. Phys. Lett.* **1999**, *75* (8), 1146−1148.
(4) Frenkel, A. L.; Pease, D. M.; Giniewicz, J.; Stern, E. A.; Brewe, D. L.; Daniel, M.; Budnick, J. *Phys. Rev. B* **2004**, 014106.
(5) Jeong, I. K.; Darling, T. W.; Lee, J. K.; Proffen, T.; Heffner, R. H.; Park, J. S.; Hong, K. S.; Dmowski, W.; Egami, T. *Phys. Rev. Lett.* **2005**, *94* (14), 147602.
(6) Kiryukin, V.; Koo, T. Y.; Ishibashi, H.; Hill, J. P.; Cheong, S. W. *Phys. Rev. B* **2003**, *67* (6), 064421.
(7) Tao, R.; Siny, I. G.; Katiyar, R. S.; Guo, R.; Bhalla, A. S. *J. Raman Spectrosc.* **1996**, *27*, 873.
(8) Siny, I. G.; Katiyar, R. S.; Bhalla, A. S. *J. Raman Spectrosc*. **1998**, *29*, 385−390.
(9) Levin, I.; Prosandeev, S. A.; Maslar, J. E. *Appl. Phys. Lett.* **2005**, *86* (1), 011919.
(10) Zheng, H.; Reaney, I. M.; Csete de Gyorgyfalva, G. D. C.; Ubic, R.; Yarwood, J.; Seabra, M. P.; Ferreira, V. M. *J. Mater. Res.* **2004**, *19* (2), 488−495.

10.1021/cm0523438 CCC: $33.50

chromator and a position sensitive detector. (Please note that the identification of any commerical product or trade name does not imply endorsement or recommendation by the National Institute of Standards and Technology.) Cu Kα_1 radiation was used. The Rietveld refinements were accomplished with the GSAS software package.[11]

The Ti−K ($h\nu$ = 4966 eV) and Zr−K ($h\nu$ = 17 998 eV) extended absorption fine structure (EXAFS) measurements were conducted at the UNICAT 33-BM facility of the Advanced Photon Source. The double crystal monochromator was operated with a pair of Si(111) crystals, a collimating mirror before the monochromator tuned to reject harmonics and to collimate the X-ray beam in the vertical direction for optimal resolution and throughput, and a vertically focusing mirror after the monochromator. The data were collected in both transmission and fluorescence using powder $CaZr_{1-x}Ti_xO_3$ samples with $x = 0$, 0.25, 0.50, 0.75, and 1. The AUTOBK code[12] was used to separate the EXAFS oscillations from the isolated atom absorption background.[13] The structural parameters for the solid-solution samples were obtained by fitting the EXAFS signal calculated with the FEFF8.20 code[14] to the experimental data. The fitting was accomplished using the IFEFFIT software.[15] The passive electron-reduction factors, $S_0{}^2$, and energy shifts, E_0, were determined using $CaTiO_3$ and $CaZrO_3$ as references.

Neutron powder diffraction patterns for the atomic PDF analyses were collected on the NDPF instrument at the Lujan Center at LANSCE. The powder samples were loaded in vanadium containers. The data were collected at ambient temperature. The data corrections were carried out using the PDFGetN software.[16] The PDF, $G(r)$, was obtained from a sine Fourier transformation of the normalized scattering intensity, $S(Q)$, according to[17]

$$G(r) = (2/\pi)\int_0^\infty Q[S(Q) - 1] \sin QrdQ$$

A $Q_{\max} = 40$ Å^{-1} was used.

Raman scattering was excited using 488 nm radiation from an argon-ion laser and instrumentation that included a holographic notch filter, a 0.5 m focal length imaging spectrometer, and a back-illuminated charge coupled device camera system ($\approx$3.5 cm^{-1} full width at half-maximum instrumental band pass). Laser radiation was focused onto the powder to produce an approximately 320 μm diameter spot with a corresponding power density of less than 18 W/cm^2. The intensities of Raman peaks in different samples were compared by using controlled additions of Li_2CO_3 as an internal standard.[9] Raman spectra of Li_2CO_3 feature a sharp peak at 1125 cm^{-1}, which was used as a reference. The sample preparation procedure was similar to that described elsewhere.[9] The statistical uncertainties in the Raman intensities were estimated from the measurements on three independently prepared samples with $x = 1/12$.

Local density functional theory structure and phonon calculations were performed for 40-atom $2a_c \times 2a_c \times 2a_c$ cells of $Ca(Zr_{1-x}Ti_x)O_3$, containing 0, 1, 2, 4, 6, 7, and 8 Ti atoms out of 8 B sites. Vanderbilt-type ultrasoft pseudopotentials were used, with semicore Ti and Zr states treated as valence states. The ionic positions of $CaTiO_3$ and $CaZrO_3$ were fully relaxed at fixed experimental lattice parameters, whereas the ionic positions and cell parameters of the other cells were relaxed under an interpolated Pulay stress (used to compensate for the local density approximation error in the lattice constant). Phonon frequencies were calculated via the frozen phonon method, as detailed elsewhere.[18]

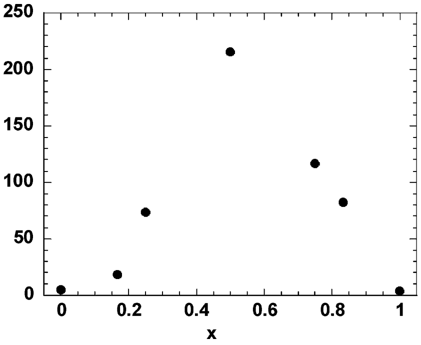

Figure 1. Gaussian contribution, reflecting a structural strain, to the X-ray line broadening as a function of Ti content in the $CaZr_{1-x}Ti_xO_3$ solid solutions. The end compounds exhibited purely instrumental broadening. The Lorentzian contribution to the line broadening was close to the instrumental value across the entire composition range. The maximum Gaussian broadening observed at $x = 0.5$ corresponds to the rms strain of $\epsilon = 6 \times 10^{-3}$.

The cells with 0, 1, 7, or 8 Ti atoms allowed only one symmetry-distinct arrangement of the B-site ions within the pseudocubic 40-atom cell. For the cells with 2 or 6 Ti atoms, one minority species ion was placed at the cell origin and one at the cell center. For the case with 4 atoms, three different B-cation arrangements were considered: (I) alternating (001) Ti and Zr layers, (II) alternating (110) Ti and Zr layers, and (III) alternating Ti and Zr layers along the ⟨111⟩ direction (i.e., a NaCl-type arrangement).

Results and Discussion

Both end compounds in this system, $CaZrO_3$[19] and $CaTiO_3$,[20] crystallize with similar room-temperature orthorhombic structures having $Pbnm$ symmetry and lattice parameters $\sqrt{2}a_c \times \sqrt{2}a_c \times 2a_c$ (where $a_c \approx 4$ Å is the lattice parameter of an ideal cubic perovskite). Deviations from the ideal cubic structure in both compounds are caused by $b^-b^-c^+$ octahedral tilting.[21] The ionic radius of Zr^{4+} (0.7 Å) is appreciably larger than that of Ti^{4+} (0.605 Å),[22] yielding significantly stronger octahedral tilting in $CaZrO_3$ than in $CaTiO_3$.

Rietveld refinements of the average $CaZr_{1-x}Ti_xO_3$ structures using X-ray powder diffraction data confirmed that all structural parameters (i.e., lattice parameters, bond distances, bond angles) vary linearly across the solid solutions. However, the structural strain (ϵ), as deduced from the Gaussian contribution to the X-ray line broadening, increases anomalously (Figure 1) with the maximum

$$\epsilon = (\pi/18\,000)\sqrt{8 \ln 2(\mathrm{GU} - \mathrm{GU_i})} = 6 \times 10^{-3}$$

---

[11] Larson, A. C.; Von Dreele, R. B. *General Structure Analysis System*; Report LAUR 86-748; Los Alamos National Laboratory: Los Alamos, NM, 1994.

[12] Newville, M.; Livins, P.; Yacoby, Y.; Rehr, J. J.; Stern, E. A. *Phys. Rev. B* **1993**, *47*, 14126.

[13] Stern, E. A.; Heald, S. M. In *Handbook on Synchrotron Radiation*; Koch, E. E., Ed.; North-Holland: New York, 1983.

[14] Zabinsky, S. I.; Rehr, J. J.; Ankudinov, A.; Albers, R. C.; Eller, M. J. *Phys. Rev. B* **1995**, *52*, 2995.

[15] Newville, M. *FEFFIT Program Manual;* unpublished.

[16] Peterson, P. F.; Gutmann, M.; Proffen, Th.; Billinge, S. J. L. *J. Appl. Crystallogr.* **2000**, *33*, 1192.

[17] Egami, T.; Billinge, S. J. L. *Underneath the Bragg Peaks: Structural Analysis of Complex Materials*; Pergamon: Oxford, U.K., 2003.

[18] Cockayne, E.; Burton, B. P. *Phys. Rev. B* **2000**, *62*, 3735.

[19] Koopmans, H. J. A.; van de Velde, G. M. H.; Gellings, P. J. *Acta Crystallogr., Sect. C* **1983**, *39*, 133.

[20] Sasaki, S.; Prewitt, C. T.; Bass, J. D.; Schulze, W. A. *Acta Crystallogr., Sect. C* **1987**, *43*, 1668.

[21] Glazer, A. M. *Acta Crystallogr., Sect. C* **1972**, *28*, 3384.

[22] Shannon, R. D. *Acta Crystallogr., Sect. A* **1976**, *32*, 751.

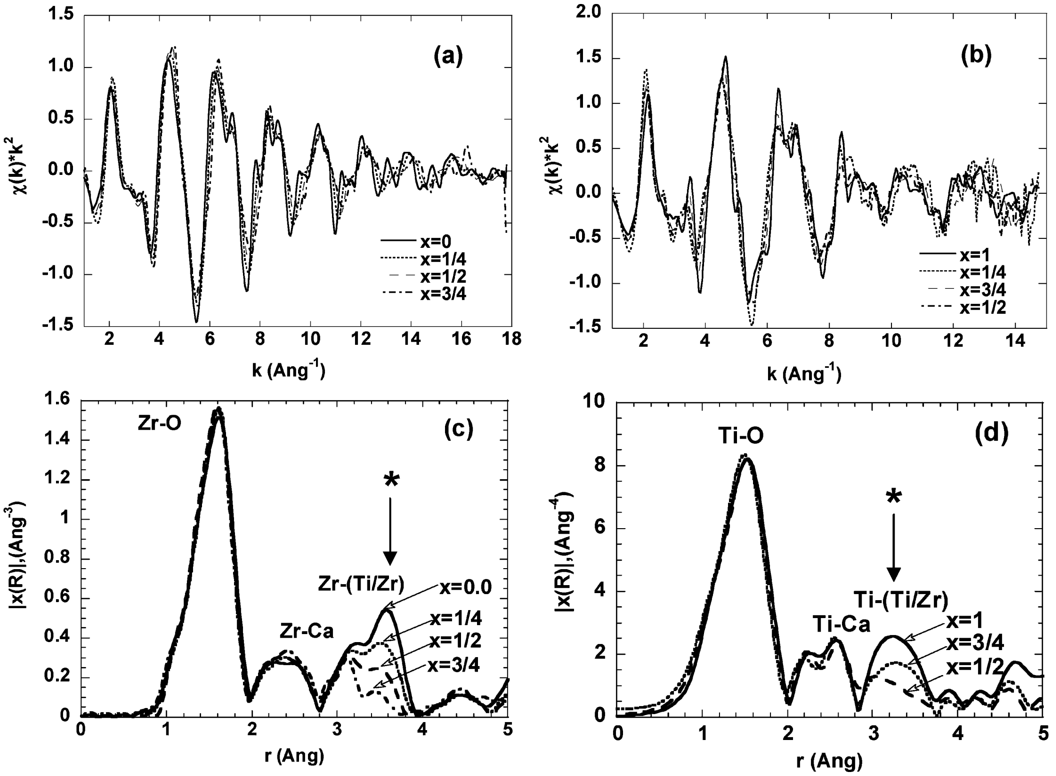

Figure 2. EXAFS signal for (a) Zr−K edge and (b) Ti−K edge for the samples with $x = 0$, 1/4, 1/2, 3/4, and 1. Magnitude of the EXAFS Fourier transformation for (c) Zr−K ($\Delta k = 1{-}17$ Å^{-1}) and (d) Ti−K ($\Delta k = 1{-}11$ Å^{-1}) edges as a function of x. Prior to a Fourier transformation, the Zr−K and Ti−K data were multiplied by k^2 and k^3, respectively. The Ti−K EXAFS data for $x = 1/4$ were too noisy beyond the first shell.

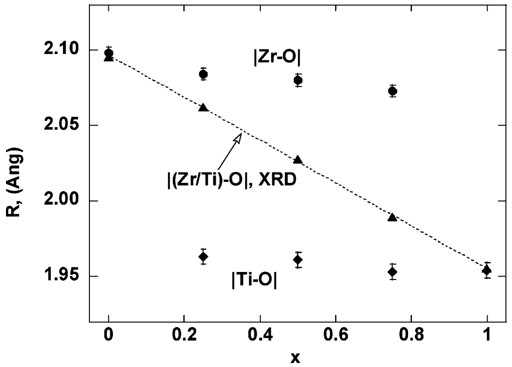

Figure 3. Zr−O and Ti−O bond distances extracted from the EXAFS first-coordination-shell fit. The average (Zr/Ti)−O bond distances obtained using Rietveld refinements are indicated as well (symbols connected with a dotted line).

observed for $x = 1/2$ (GU_i is the instrumental Gaussian contribution). The dependence $\epsilon(x)$ is asymmetric with less strain introduced by dissolving a smaller Ti cation in the $CaZrO_3$ lattice.

The EXAFS signal in *k*-space and the magnitudes of the EXAFS Fourier transformations for the Ti−K and Zr−K edges are summarized in Figure 2. Fitting FEFF calculations to the first B−O coordination shell demonstrated that the Zr−O and Ti−O bond distances remain distinct in the solid solutions, close to those in the respective end compounds (Figure 3). However, a small yet systematic variation of these bond lengths with composition is observed: the Zr−O distance decreases with increasing Ti content, whereas the Ti−O distance increases with the addition of Zr. The observed trends are similar to those reported previously for the solution-processed $CaZr_{1-x}Ti_xO_3$,[23] as well as for other non-oxide solid-solution systems, including ternary $Ga_{1-x}In_xAs$[24,25] and binary $Si_{1-x}Ge_x$.[26] The present first-principles calculations also predict the Ti−O and Zr−O bond lengths to decrease from 2.00 to 1.96 Å and from 2.11 to 2.08 Å, respectively, with the Ti fraction increasing from near-zero to 1. The Debye−Waller factors $\sigma_{Zr-O} = 0.003(1)$ Å^2 and $\sigma_{Ti-O} = 0.005(1)$ Å^2 vary little with composition, which suggests little change in the distribution of the Zr−O and Ti−O bond distances for each of the solid solutions.

The effect of composition on the EXAFS data is most pronounced in the third peak at $r \approx 3.9$ Å (indicated with an asterisk in Figure 2). The intensity of this peak decreases with increasing *x* for both Ti−K and Zr−K data. According to the FEFF calculations for $CaZrO_3$ and $CaTiO_3$, the third peak contains contributions from several types of scattering paths, including (1) single scattering on the neighboring Zr/Ti atoms (i.e., **Zr** ↔ Zr or **Ti** ↔ Ti, where the absorbing atoms are indicated in bold), (2) single scattering on the oxygen atoms that belong to the adjacent octahedra, (3) collinear multiple scattering on the oxygen atoms, and (4) noncollinear multiple scattering, such as **Zr** → O → Zr → **Zr** or **Ti** → O → Ti → **Ti**. Because of these non-collinear scattering paths, the intensity of the $r \approx 3.9$ Å peak varies with the bond angle B−O−B (magnitude of octahedral tilting).[27] In the solid solutions of $CaZr_{1-x}Ti_xO_3$, the intensity

---

(23) Xu, J.; Lind, C.; Wilkinson, A. P.; Pattanaik, S. *Chem. Mater.* **2000**, *12* (11), 3347−3355.

(24) Mikkelsen, J. C.; Boyce, J. B., Jr. *Phys. Rev. Lett.* **1982**, *49* (19), 1412−1415.

(25) Woicik, J. C. *Phys. Rev. B* **1998**, *57*, 6266−6269.

(26) Woicik, J. C.; Miyano, K. E.; King, C. A.; Johnson, R. W.; Pellegrino, J. G.; Lee, T.-L.; Lu, Z. H. *Phys. Rev. B* **1998**, *57*, 14592−14595.

(27) Teo, B. K. *J. Am. Chem. Soc.* **1981**, *103*, 3990.

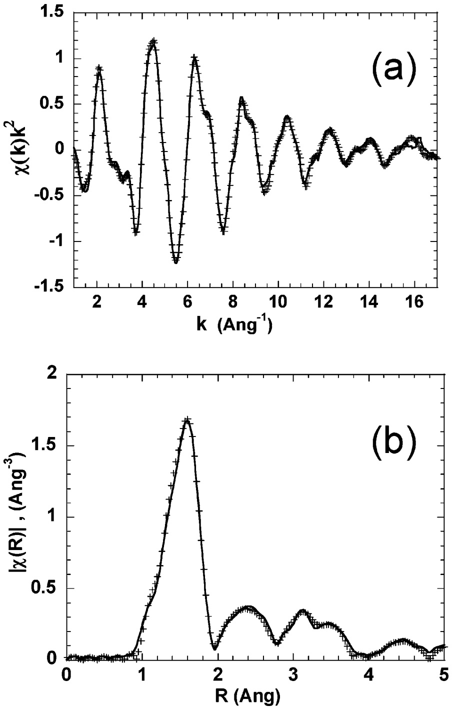

Figure 4. (a) Zr−K EXAFS signal and (b) magnitude of the EXAFS Fourier transformation (for $x = 0.50$ (crosses) and the average of the $x = 1/4$ and $x = 3/4$ (solid line)). The agreement between the two quantities suggests a near-random distribution of Ti and Zr in the $x = 1/2$ sample.

of this peak additionally depends on the probability, p_{Zr}, of finding a Zr atom next to Ti (on the B-site sublattice) or vice versa; that is, this intensity is directly related to the value of the B-cation short-range order parameter $\alpha = 1 - p_{Zr}/(1 - x)$. Unfortunately, strong correlations between the tilting angles, α, and D−W factors associated with different scattering paths preclude reliable co-refinement of all these parameters.

A semiquantitative insight into the distribution of Ti and Zr can be obtained by comparing a 1:1 mixture of the EXAFS data for $x = 1/4$ and $x = 3/4$ to that for $x = 1/2$.[23] For a random Zr/Ti distribution, the average of the $x = 1/4$ and $x = 3/4$ compositions contains the same number of Zr nearest neighbors around Ti (and vice versa) as that of the $x = 1/2$ composition and, therefore, a close match between $^1/_2[|\chi(r)_{x=1/4}| + |\chi(r)_{x=3/4}|]$ and $|\chi(r)_{x=1/2}|$ is expected. A similar geometry of the Ti−O−Ti, Ti−O−Zr, and Zr−O−Zr links in different samples is assumed. Indeed, a good agreement of these quantities is observed in Figure 4 for Zr−K EXAFS, thus suggesting a near-random distribution of Ti and Zr.

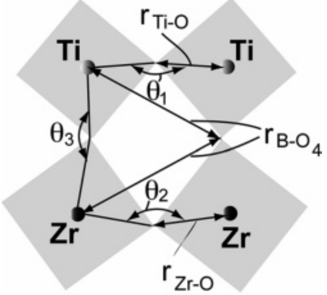

Figure 5. Structural model used in the EXAFS fit. (The Ca atoms are not shown.) The independent variables included the following: bond distances r_{Zr-O}, r_{Ti-O}, r_{B-O4}, r_{Ti-Ca} (×3), r_{Zr-Ca} (×3); bond angles θ_1 = Ti−O−Ti, θ_2 = Zr−O−Zr; D−W factors σ_{Zr-O}, σ_{Ti-O}, σ_{B-O4}, $\sigma_{Ti/Zr-Ti/Zr}$, and $\sigma_{Ti/Zr-Ca}$. The angle θ_3 = Ti−O−Zr was set as $^1/_2(\theta_1 + \theta_2)$. The Ca displacements were assumed to occur parallel to the ⟨110⟩ direction of the ideal cubic perovskite cell (i.e., a-axis of CaZrO$_3$ or CaTiO$_3$), yielding three distinct (Ti/Zr)−Ca distances.

The structural parameters (Figure 5) were obtained for $x = 1/2$ by fixing the p_{Zr} at different values and using a simultaneous fit of the FEFF calculations to the Zr and Ti data. Constraints were applied, where possible, to minimize the number of independent variables (see the caption for Figure 5). For example, the D−W factors for the multiple-scattering (three- and four-leg) paths involving B-cations and oxygen atoms were constrained to be equal to the D−W factors for corresponding single-scattering B ↔ O paths. A single distance and the D−W factor were used for the single-scattering path between either Ti or Zr and the next-nearest neighbor O atom (i.e., $r_{Ti-O4} = r_{Zr-O4}$, $\sigma_{Ti-O4} = \sigma_{Zr-O4}$, Figure 5). Similarly, a single D−W factor was used for the Ti ↔ Ca and Zr ↔ Ca paths. A linear interpolation between the scattering amplitudes calculated for the B−O−B angles of 160 and 144° was sufficient to account for the angular dependence of the amplitude for the noncollinear paths. The best fits combined with the most reasonable values of the D−W factors were obtained for p_{Zr} values between 0.40 and 0.52 (Figure 6), which is consistent with a near-random distribution of Zr and Ti, as suggested by Figure 4. Three bond angles, Zr−O−Zr, Ti−O−Ti, and Zr−O−Ti, were required because attempts to use a single common angle for the distinct B−O−B links yielded significantly poorer fits. The Zr−O−Ti angle was constrained to be the average of the Zr−O−Zr and Ti−O−Ti angles. The refined angles (160 ± 2.5° for Ti−O−Ti and 143 ± 1.5° for Zr−O−Zr) were close to their values in the corresponding end compounds. Such a three-modal distribution of the tilting angles can be attributed to a presence of the Zr-rich, Ti-rich, and 50:50 Ti:Zr localized regions; similar distributions of the tilting angles were reported from the theoretical modeling of Pb(Zr,Ti)O$_3$ solid solutions.[28] According to our results, the large structural strain in the $x = 0.50$ sample is accommodated by the distribution of the tilting angles. The distortion of the O−O distances, which could also contribute to the strain accommodation, cannot be ascertained from the Zr−K/Ti−K edge EXAFS; however, this complementary information was obtained from the total-scattering PDF.

The atomic PDF, $G(r)$, derived from the neutron scattering for the CaZr$_{1-x}$Ti$_x$O$_3$ solid solutions, is shown in Figure 7. Because Ti has a negative neutron-scattering cross section, the PDF peaks representing the Ti−Zr, Ti−O, and Ti−Ca correlations appear to be negative. The positions and widths of the first-shell Ti−O and Zr−O peaks are nearly independent of composition, consistent with the EXAFS observations. Similar to the EXAFS data for $r < 6$ Å, the $G(r)$ of the $x = 0.5$ sample is closely reproduced by a 1:1 mixture of the $G(r)$ for the Zr-rich ($x = 1/4$) and Ti-rich ($x = 3/4$) samples. These results are consistent with the near-random distribution of Zr and Ti in the B−B nearest-neighbor shell.

---

(28) Grinberg, I.; Cooper, V. R.; Rappe, A. M. *Phys. Rev. B* **2004**, *69*, 144118.

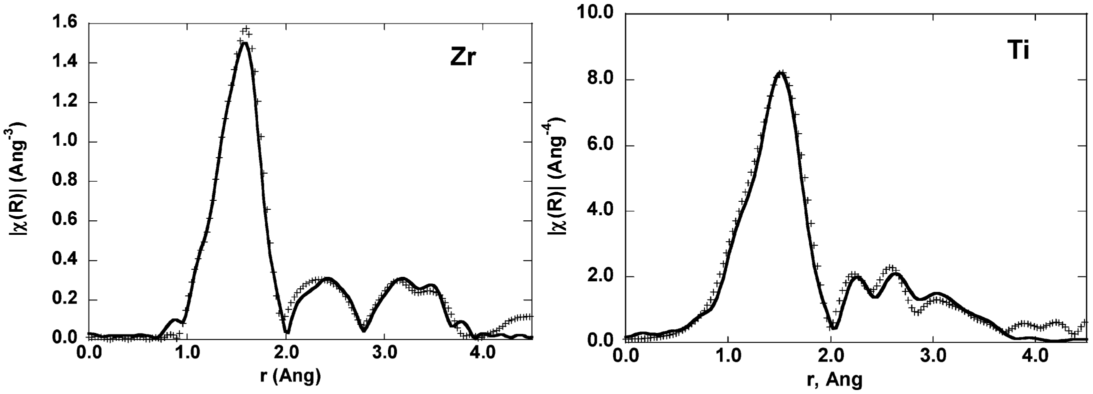

Figure 6. Experimental (crosses) and fitted (line) magnitude of EXAFS Fourier transform for the Ti and Zr data at $x = 1/2$. A simultaneous fit to both data sets was used. The fitting range was from 1.1 to 4.2 Å. The number of independent points and structural variables was 68 and 16, respectively.

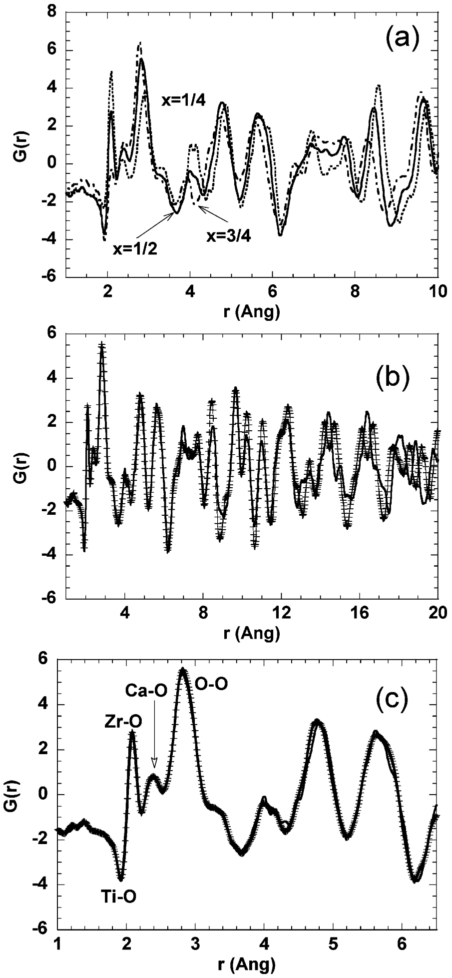

Figure 7. (a) Portions of the total PDF, as derived from neutron scattering, for samples with $x = 1/4$, $x = 1/2$, and $x = 3/4$; (b) 1:1 average of the PDF for $x = 1/4$ and $x = 3/4$ superimposed onto the PDF for $x = 1/2$; (c) low-r portion of panel b.

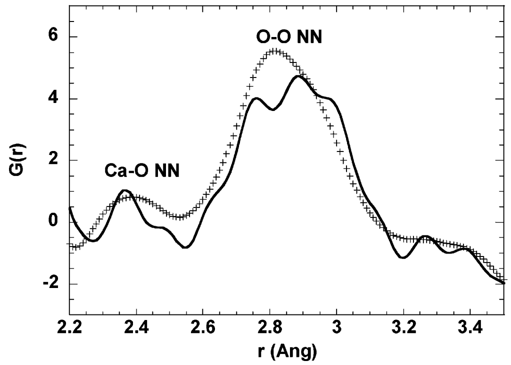

Figure 8. Portion of the neutron PDF containing the O−O peak. (Crosses) PDF for $x = 1/2$; (solid line) average PDF for $CaZrO_3$ ($x = 0$) and $CaTiO_3$ ($x = 1$).

For $r > 6$ Å, the PDF reflects an average rather than a local structure.

The PDF peak at $r \approx 2.8$ Å is determined primarily by the nearest-neighbor O−O correlations, with the Ca−O correlations contributing to the tails of this peak. The overall spread of the O−O distances in the solid solutions is similar to that expected for a mixture of the regular $[ZrO_6]$ and $[TiO_6]$ octahedra; however, the O−O correlations in the solid solutions yield a single nearly symmetric peak instead of several maxima for the $CaTiO_3$−$CaZrO_3$ mixture (Figure 8). These observations can be attributed to a broader asymmetric distribution of the O−O distances for the $[ZrO_6]$ and $[TiO_6]$ octahedra in the solid-solution samples. In particular, in the $x = 0.50$ sample, the distributions of the O−O distances for the $[ZrO_6]$ and $[TiO_6]$ octahedra are skewed toward shorter and longer distances, respectively. The distortion of octahedra is such that it preserves a narrow distribution of the B−O distances (e.g., bending). The results of a detailed PDF modeling using a reverse Monte Carlo algorithm will be reported separately.

The Raman spectra of the $Ca(Zr_{1-x}Ti_x)O_3$ solid solutions are summarized in Figure 9. The spectra for all samples except the end compounds feature a high-frequency band around ~780 cm^{-1} (Figure 9a,c). For relatively dilute concentrations of the solute B-cations (<0.25% on either side), this band features a doublet (labeled as **L** and **E** for reasons described below), whereas for the concentrations around $x = 0.50$, the doublet is replaced by a single, broad, somewhat asymmetric peak (Figure 9b,c). First-principles methods were used to understand the nature of these high-frequency peaks.

First-principles phonon calculations for all 40-atom supercells studied, except for the one with equal Zr and Ti concentrations, revealed localized oxygen octahedron breathing modes around the minority species. These modes are Raman-active by symmetry; therefore, one of the two peaks observed in the spectra for the dilute solid solutions (Figure 9b,c) was attributed to a localized (**L**) mode. Extended (**E**) oxygen octahedron breathing modes were identified in all cases, even for the cells with equal Zr and Ti concentrations,

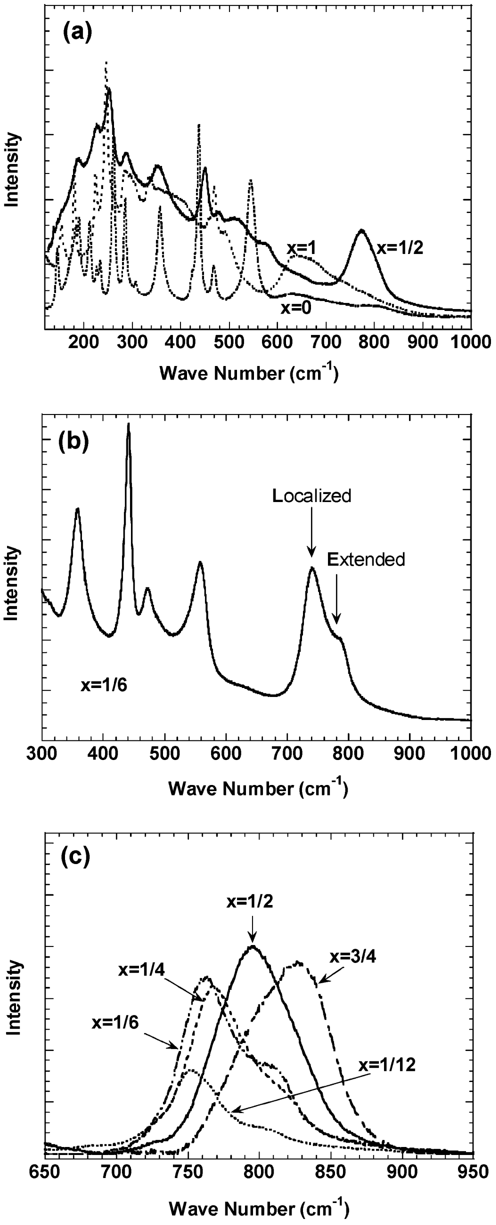

Figure 9. Raman spectra of the CaZr$_{1-x}$Ti$_x$O$_3$ samples with (a) $x = 0$, $x = 1$, and $x = 1/2$ and (b) $x = 1/6$. A clearly resolved high-frequency doublet (**L** + **E**) is observed. (c) Portions of Raman spectra showing the evolution of the high-frequency peak with composition.

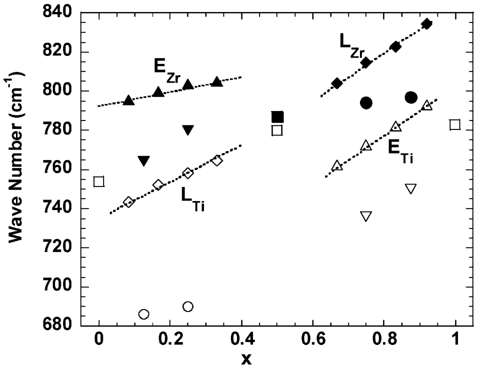

Figure 10. Compositional dependence of experimental and calculated Raman frequencies for the localized (**L**) and extended (**E**) breathing modes, which involve octahedra centered on Ti (**L**$_{Ti}$, **E**$_{Ti}$) and Zr (**L**$_{Zr}$, **E**$_{Zr}$). The points representing the experimental frequencies are connected by lines. The calculated frequencies are indicated using inverted triangles and circles. For $x = 0.50$, in which no distinction can be made between the localized and extended modes, a single frequency is given (solid square, experimental; open square, calculated).

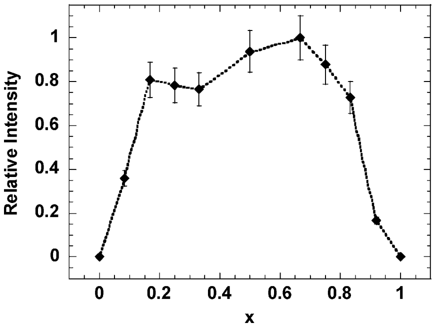

Figure 11. Compositional dependence of Raman intensities for the high-frequency breathing mode peak. The integral intensities (**L** + **E**) are shown.

and were the obvious candidates for explaining the second peak for the dilute solid solutions (Figure 9c). The first-principles frequency results for the different breathing modes are shown in Figure 10 and were used to assign the Raman modes observed experimentally. (First-principles calculations were found to underestimate the frequency of the symmetric breathing mode by 5−10% even for well-ordered complex perovskites.[29] We believe this error is due in part to the fact that the calculations assume zero temperature, whereas the experiment is performed at room temperature, where the octahedral tilting angles are smaller). Near the $x = 1/2$ composition, in which no distinction can be made between the solute and host cations, the predicted frequency of the **E**-type modes ranges from 766 to 791 cm^{-1}, depending on the Ti−Zr ordering. In the case of Ti−Zr disorder, with a variety of local environments, the Raman peak is expected to be broad. The experimental frequencies of both localized and extended breathing modes increase with increasing Ti content (Figure 10). First-principles calculations also predict that the frequencies of these modes increase with the addition of Ti. This effect of composition on the frequencies of breathing-type oxygen vibrations can be attributed to the strengthening of the B−O bonds with increasing Ti content, as evidenced by the shortening of both Zr−O and Ti−O bonds (Figure 3). The octahedral tilting angle decreases with increasing Ti content, causing additional hardening of breathing-like oxygen vibrations.

The integrated Raman intensities ($I = I_L + I_E$) associated with the breathing-like oxygen vibrations are summarized in Figure 11 (the intensities were normalized to the intensity of the reference Li$_2$CO$_3$ peak). The intensity increases steeply, with the solute content (either Zr or Ti) increasing from 0 to 1/6, and remains relatively flat for the solute concentrations ranging from 1/6 to 5/6. This flattening of the Raman intensity over a broad concentration range could be attributed to a weak clustering of the B-cations (i.e., positive short-range order parameter) which reduces the number of Zr−O−Ti links; however, in the absence of a theoretical modeling of Raman intensities in disordered solid solutions, the exact reasons for such a compositional dependence remain unclear.

The width of the breathing-mode peak in CaZr$_{0.5}$Ti$_{0.5}$O$_3$, 65 cm^{-1}, is about 50% larger than the typical line widths of similar Raman peaks in well-ordered perovskites (40 cm^{-1}).[9,29]

However, 65 cm^{-1} is comparable to the width of the breathing mode peak commonly reported for $Pb(Mg_{1/3}Nb_{2/3})O_3$ (52−62 cm^{-1}), which, in contrast to $CaZr_{0.5}Ti_{0.5}O_3$, exhibits a pronounced nanoscale ordering of Mg and Nb.[30,31] Therefore, a comparison of the extent of the B-site ordering in chemically distinct systems using Raman line widths can be misleading. In a given system, stronger short-range order is expected to produce a sharper breathing-mode Raman peak.

Conclusions

The dissimilar ionic sizes of Zr and Ti ($\Delta R = 0.1$ Å) generate significant structural strain in the $Ca(Zr,Ti)O_3$ solid solutions. According to the local structure analyses, this strain is accommodated by the distribution of the octahedron tilting angles and some bending of the oxygen octahedra. The nearest-neighbor Zr−O and Ti−O bond distances in the solid solutions remain close to those in the respective end compounds, with no detectable broadening of their distributions. Our results suggest that the $Ca(Zr,Ti)O_3$ solid solutions synthesized here exhibit a near-random distribution of Ti and Zr (the absolute value of the B-cation short-range order parameter is less than 0.1). Raman spectra of such nearly disordered solid solutions still exhibit a high-frequency Raman feature attributed to a breathing-like motion of oxygen octahedra. For relatively dilute solid solutions (<25 at. %), a doublet is observed instead of a single peak. Based on ab initio calculations of the phonon spectra, the doublet was attributed to localized and extended breathing-like modes associated with the oxygen breathing around the minority and majority B-cations, respectively. In the concentrated solid solutions ($x \approx 0.50$), this high-frequency doublet is replaced by a single broad Raman peak. According to our results, the breathing-mode Raman peak does not imply the existence of a significant short-range chemical order in the sample.

Acknowledgment. The authors are grateful to Jenia Karapetrova of the Advanced Photon Source, Argonne National Laboratory, and to Thomas Proffen of Los Alamos National Laboratory for technical assistance with the EXAFS and neutron-scattering measurements, respectively. The facility at the Advanced Photon Source (APS) is supported by the U.S. Department of Energy under Award DEFG02-91ER45439, through the Frederick Seitz Materials Research Laboratory at the University of Illinois at Urbana−Champaign, the Oak Ridge National Laboratory (U.S. Department of Energy Contract DE-AC05-00OR22725 with UT-Battelle LLC), the National Institute of Standards and Technology (U.S. Department of Commerce), and UOP LLC. The APS is supported by the U.S. Department of Energy, Basic Energy Sciences, Office of Science, under Contract W-31-109-ENG-38.

CM0523438

---

(29) Prosandeev, S. A.; Waghmare, U.; Levin, I.; Maslar, J. *Phys. Rev. B* **2005**, *71*, 214307.

(30) Idink, H.; White, W. B. *J. Appl. Phys*. **1994**, *76* (3), 1789−1793.

(31) Jiang, F.; Kojima, S.; Zhao, C.; Feng, C. *J. Appl. Phys*. **2000**, *88* (6), 3608−3612.